

Imaging of interferometric On-The-Fly observations (I): context and discussion of possible methods*

N. Rodriguez-Fernandez (IRAM), Jerome Pety (IRAM), Frederic Gueth (IRAM)

15 6 2009

Abstract

We discuss the measurement equation for interferometric observations of fields larger than the primary beam of the antennas, both for standard “pointed” mosaics and for mosaics observed in *on-the-fly* (OTF) mode. The main advantages of using the OTF mode are a gain of observing time and a higher homogeneity of the dataset. OTF mosaicing is similar to classical stop-and-go mosaicing but the effective beam when observing OTF is not exactly the primary beam of the antennas. We show that the effective beam is similar to the primary beam when the scanning rate is better than Nyquist. We review different techniques to image and deconvolve mosaic data, in particular the Ekers & Rots 1979 (ER79) scheme, which consist in Fourier transforming the visibility function with respect to the scanning coordinate. We discuss how to implement an OTF-optimized imaging algorithm to deal with the mosaic data as a whole based on the ER79 scheme. Finally we discuss observing time and mosaic size constrains for OTF observations.

*This work is funded by the EU FP6 grant “ALMA enhancement”.

Contents

1	Introduction	3
2	Wide field observations: mosaics	4
2.1	Mosaicing measurement equation	4
2.2	The effective beam for on-the-fly observations	5
2.3	On the need of short-spacings	7
3	Imaging techniques for mosaics	9
3.1	Basic image synthesis	9
3.1.1	Gridding and sampling	10
3.2	Mosaic imaging as linear combination of individual images	10
3.3	An alternative method to image mosaic data: constructing a global uv -plane using the Ekers & Rots scheme	12
3.3.1	The Ekers & Rots scheme versus real interferometers	13
3.4	Comparison of the two methods	14
4	Mosaic size and observing time limitations for OTF observations	15
4.1	Earth rotation: different uv coverages for the different fields/integrations	15
4.2	Fringe tracking: coherence loss when using a fixed phase-center	18
5	Imaging techniques for OTF mosaics	19
5.1	One dirty image per dump, linear combination and joint deconvolution	19
5.2	Constructing a global uv -plane and dirty image	20
5.2.1	Beginning by Fourier Transforming the visibility maps	22
5.2.2	Beginning by gridding the independent uv planes	23
6	Discussion of the different methods and summary	25
7	Bibliography	27

1 Introduction

ALMA has been designed to be an extremely powerful imaging instrument by a detailed choice of the array configurations (Ge & Jing Ping 1992, Holdaway 1996, 1997; Kogan 1997; Boone 2002). However, mapping an extended source will be complex by two effects:

- Lack of the short spacings: as any interferometer, ALMA will filter out the shortest spatial frequencies, which contain the information that describes large-scale structure in the target field; this calls for an independent way to measure this information. The ALMA Compact Array (ACA), an enhancement consisting of an array of twelve 7-m dishes and four 12-m dishes to be used in single-dish mode, will provide the short-spacings information to be merged with the ALMA datasets.
- The limited field-of-view (FOV): the FOV of an interferometer is limited by the primary beams of the antennas, which scales with the inverse of the observing frequency: for ALMA, the FOV is $\sim 22''$ at 230 GHz. As a consequence, many of ALMA's science targets will be extended over many primary beam diameters. For instance, Fig. 1 shows the ALMA FOV overlaid on maps of the galaxy M51 and the molecular outflow of the protostar L1157. At the highest frequencies, structures larger than $5''$ arcsec will be resolved out by the interferometer.

To overcome the limitations of an interferometer's narrow FOV, the solution adopted with existing instruments is to observe mosaics of adjacent, overlapping fields, which are further combined in the data reduction software to produce an image of an extended area in the sky. This observing mode can be described as "stop-and-go" or "point-and-shoot" mosaicing. However, a more promising observing mode is the so-called on-the-fly (OTF) mapping, in which the antenna beams are continuously swept across the entire region of interest. The two main advantages of this technique are:

- Gain of observing time: since data are acquired continuously; there is no time lost in the "stop and observe, then slew to the next field" procedure that characterizes "stop-and-go" mosaicing. This allows to observe larger fields (Holdaway & Foster 1994, Holdaway & Rupen 1995).
- Data homogeneity: while in a classical mosaic each field may have different properties (in terms of calibration or sensitivity), OTF observations will cover the entire region faster and thus under much more similar weather and instrumental conditions than stop-and-go observations.

OTF has proven to be a powerful observing mode with single-dish mm-wave telescopes, such as the IRAM 30-m, but has yet to be implemented on an interferometer. Nevertheless, OTF is promising, so that it is planned as a standard ALMA observing mode. However, OTF mosaicing poses several major challenges for the data processing algorithms. Image and deconvolution algorithms for stop-and-go mosaics is done to great extend field by field, for instance, producing independent *dirty* images that are combined before perform a joint deconvolution. One possibility that has to be explored for OTF mosaics is to use that classical scheme with a very high number of fields. In addition, more sophisticated algorithms can be developed to optimize the data processing, for instance, a method in which data points are Fourier transformed with

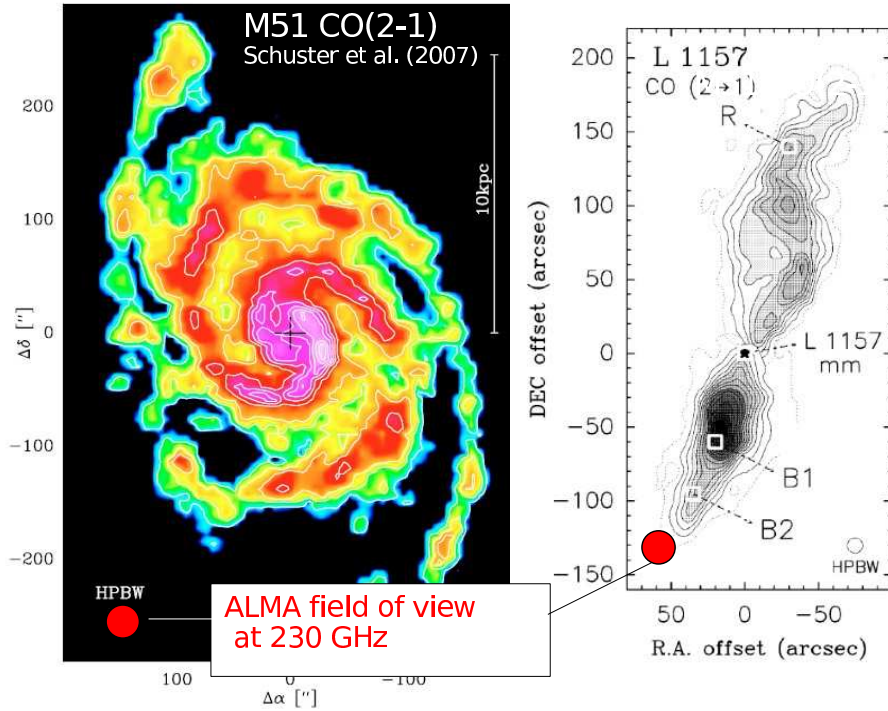


Figure 1: Full width at half maximum of the primary beam of the ALMA antennas at 230 GHz overlaid on maps of the galaxy M51 and the molecular outflow of the protostar L1157.

respect to their angular coordinates in the sky, in order to compute a global uv-plane containing the whole information of the mosaic.

In this document we present the measurement equation for stop-and-go and OTF mosaics and we compute the effective beam for OTF observations (Sect. 2). In Sect. 3 we review the classical image synthesis methods for single fields and stop-and-go mosaics. We also introduce the Ekers & Rots (1979, hereafter ER79) scheme to deal with mosaic data, which is very well adapted to OTF mosaics and can represent an improvement in data processing algorithms. Observing time and map size constrains for OTF mosaicing are discussed in Sect. 4. Different possibilities to image OTF data are discussed in Sect. 5, including a classical scheme (Sect. 5.1) and ER79-based methods (Sect. 5.2). Finally, we present a summary and the conclusions in Sect. 6.

2 Wide field observations: mosaics

2.1 Mosaicing measurement equation

The interferometer measures the visibility function, which is the Fourier Transform of the sky brightness distribution apodized by the primary beam of the antennas.

$$V(u, v) = \iint B(l, m) I(l, m) e^{-i2\pi(ul+vm)} dl dm \quad (1)$$

In the following we will simplify the notation using vectors $\mathbf{u} \equiv \vec{u} \equiv (u, v)$, $\mathbf{l} \equiv \vec{l} \equiv (l, m)$. In

addition we will use a *tilde* to denote the Fourier pair of a given function ($\tilde{B}(\mathbf{u}) \equiv FT[B(\mathbf{l})]$). Using this notation one can write the visibility as:

$$V(\mathbf{u}) \equiv \widetilde{B} I \equiv \int B(\mathbf{l}) I(\mathbf{l}) e^{-i2\pi\mathbf{u}\mathbf{l}} d\mathbf{l} \quad (2)$$

If the telescopes are not pointing to the origin of the reference system (usually the “center” or a central position of the source) but to \mathbf{l}_p , the function describing the primary beam should be shifted and the visibility should be expressed as a function of both \mathbf{u} and \mathbf{l}_p :

$$V(\mathbf{u}, \mathbf{l}_p) = \int B(\mathbf{l} - \mathbf{l}_p) I(\mathbf{l}) e^{-i2\pi\mathbf{u}\mathbf{l}} d\mathbf{l} \quad (3)$$

For a single dish $\mathbf{u} = 0$ and:

$$V(0, \mathbf{l}_p) = \int B(\mathbf{l} - \mathbf{l}_p) I(\mathbf{l}) d\mathbf{l} \quad (4)$$

That is, the visibility at the phase center is the total flux of the source and we have the usual convolution equation for single-dish mapping.

Observing “on-the-fly” Equation 3 assumes that the mosaics are done using a *point-and-shoot* or *stop-and-go* (hereafter, SAG) technique, i.e., where the antennas are pointed to a sky position and they integrate for a given time before going to another sky position to take more data. One could think of an observing mode where data are collected as the antennas move scanning the sky continuously. This observing mode is usually known as *on-the-fly* (OTF).

If the antennas are moving while collecting data the parameter l_p is not fixed but it varies with time. Thus the visibility equation should be written as:

$$V(\mathbf{u}, \mathbf{l}_p) = \int_{t_0 - \frac{t_d}{2}}^{t_0 + \frac{t_d}{2}} dt/t_d \int dx B(\mathbf{l} - \mathbf{l}_p(t)) I(\mathbf{l}) e^{-i2\pi\mathbf{u}\mathbf{l}} \quad (5)$$

Where t_d is the dumping time. By convenience we have defined the reference time t_0 at the middle of the OTF integration. Assuming that the spatial frequency \mathbf{u} is constant over the integration time, OTF mosaicing is similar to stop-and-go mosaicing although with an effective beam B_{eff} given by:

$$B_{eff}(\mathbf{l}) = \int_{t_0 - \frac{t_d}{2}}^{t_0 + \frac{t_d}{2}} dt B(\mathbf{l} - \mathbf{l}_p(t))/t_d \quad (6)$$

2.2 The effective beam for on-the-fly observations

OTF mosaicing is similar to stop-and-go mosaicing with an effective beam B_{eff} given by Eq. 6. In this section, we compute the effective beam assuming that $|\mathbf{l}_p(t)|$ changes linearly with time ($|\mathbf{l}_p(t)| = v_{scan}t_d$). Figure 2 shows a comparison of $B(\mathbf{l})$ (assumed to be a Gaussian with FWHM of 44”) and $B_{eff}(\mathbf{l})$. The scanning velocity v_{scan} is set to 10 arcsec/sec. With about four integrations within the FWHM of the primary beam (which in this example are achieved with $t_d = 1$ s) the effective beam is almost equivalent to the primary beam. The difference between B and B_{eff} starts to be significant when there are less than two integrations per FWHM of the primary beam (i.e., when the sampling is worse than the Nyquist rate, which in this example correspond to dumping times larger than 2 s).

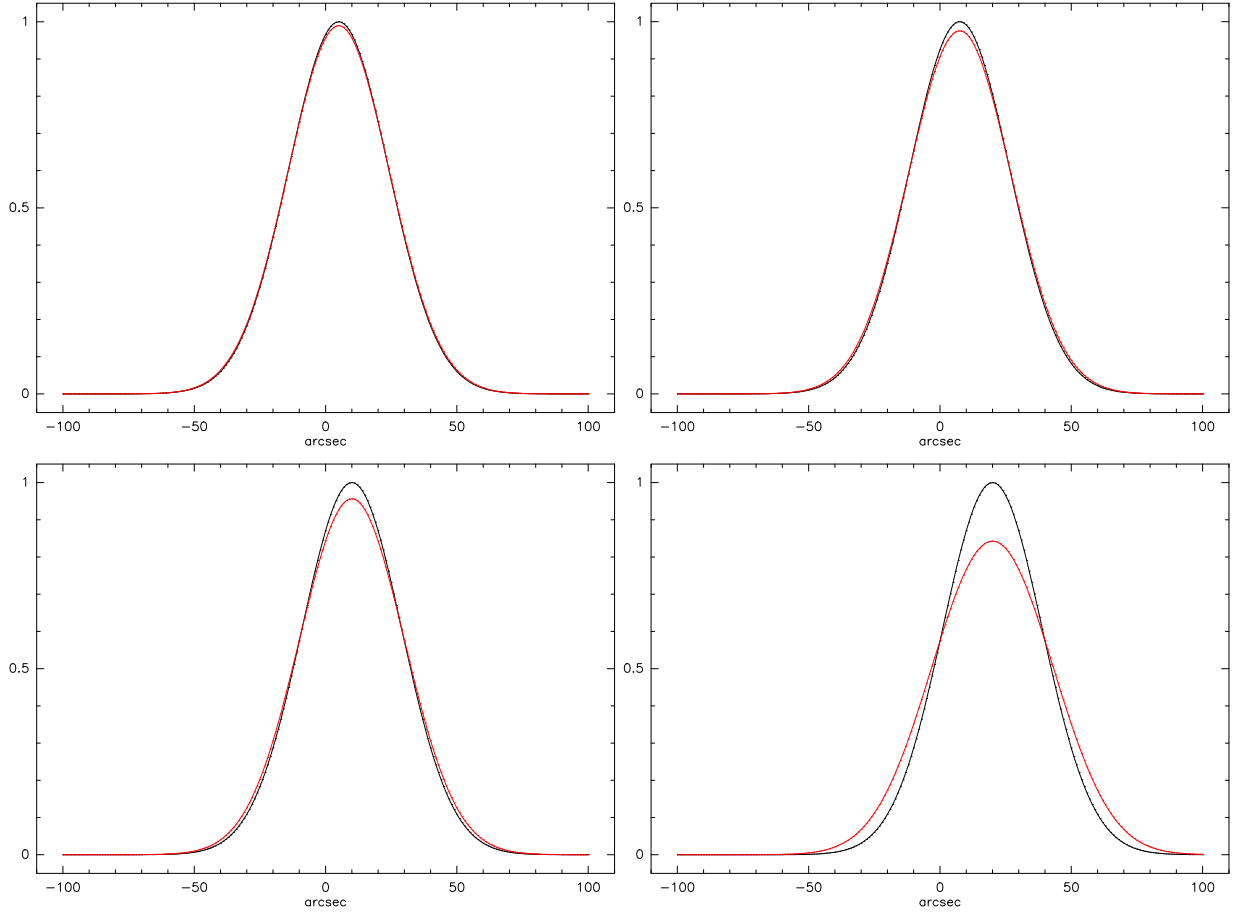


Figure 2: Comparison of $B(l)$ (black) given by a Gaussian of FWHM of $44''$ and $B_{eff}(l)$ (red) as given by Eq. 6 for $v_{scan} = 10$ arcsec/sec and $t_d = 1$ s (upper left panel), $t_d = 1.5$ s (upper right panel), $t_d = 2$ s (lower left panel), and $t_d = 4$ s (lower right panel).

In order to better understand the shape of the effective beam it is useful to obtain the equation in the Fourier space. Assuming that $t_0 = 0$, one can change the integral limits by introducing a boxcar function ($\Pi(x) = 1$ if $|x| < 1/2$ and 0 elsewhere):

$$B_{eff}(l) = \int_{-\infty}^{\infty} \frac{dt}{t_d} \Pi(t/t_d) B(l - l_p(t)) \quad (7)$$

If $l_p(t)$ changes linearly with time ($l_p(t) = v_{scan}t_d$) is easy to shown that Eq. 7 is a convolution:

$$B_{eff}(l) = \frac{1}{v_{scan}t_d} B(l) * \Pi\left(\frac{l}{v_{scan}t_d}\right) \quad (8)$$

And therefore in the Fourier Plane we have

$$\tilde{B}_{eff}(u) = \tilde{B}(u) \cdot \text{sinc}(uv_{scan}t_d) \quad (9)$$

Where $\tilde{B}(u)$ is the FT of the primary beam or the autocorrelation of the antenna illumination pattern. To avoid sensitivity losses, the first null of the sinc function should be well outside the region where $B(u) \gg 0$. The slew distance should be much less that the primary beam size.

Figure 3 show the results of some simulations with a primary beam of 44", a scanning velocity of 10 arsec/sec and dumping times of 1, 1.5, 2 and 4 s. The total size and the spacing in the Fourier space have been obtained assuming a spacing in the image plane of $\delta l = v_{scan}t_d$. The effective beam is very close to the primary beam with three to four integrations within the FWHM of the primary beam ($t_d = 1$ or 1.5 s).

2.3 On the need of short-spacings

If one is interested in mosaics it is to do wide field imaging. In this case, one would like to map the extended structure of the source corresponding to the low spatial frequencies. Unfortunately, in a multiplicative interferometer the lowest frequencies are not measured and structures more extended than $\sim 1/3$ - $1/2$ of the primary beam are filtered out. This is an obvious limitation to image large fields with an interferometer doing mosaics. Independently of the method used to do the mosaic (SAG or OTF), the observer will be interested in adding the short-spacing information.

A more compact array of smaller antennas can be used to measure the source visibility for frequencies inside the inner hole of the ALMA uv coverage. This is the goal of the Atacama Compact Array (ACA). ALMA and ACA imaging capabilities have been already studied in depth (Yun 2001, Morita 2001, Pety, Gueth & Guilloteau 2001a, 2001b, Tsutsumi et al. 2004). The visibility for the innermost frequencies can be obtained using the four 12m antennas of ACA as single dishes by mapping the source and computing *pseudovisibilities*. This is done deconvolving the sky brightness distribution from the single dish beam, multiplying by the interferometer primary beam and Fourier transforming to derive the visibilities corresponding to the low spatial frequencies. A detailed study of the pseudovisibility method and the single-dish observing time required to obtain a good combined dirty beam (and combined images) has been presented in Rodríguez-Fernández, Pety & Gueth (2008).

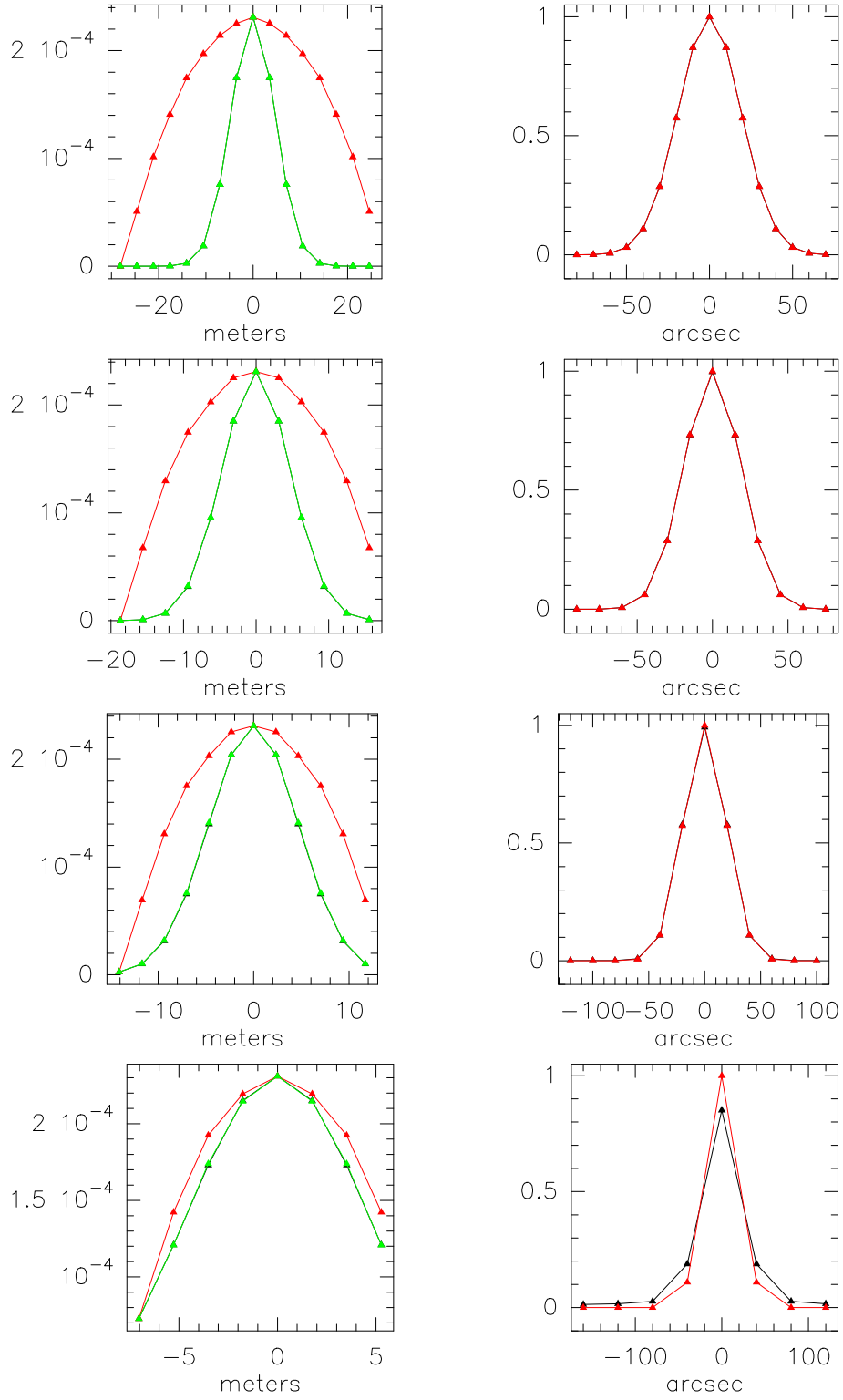


Figure 3: The left panels show $B(u)$ (green), $\text{sinc}(uv_{scan}t_d)$ (red) and their product (black). The right panels show the effective beam $B_{eff}(l)$ (black) and the primary beam $B(l)$ (red). Upper panels give results for $t_d = 1$ s, middle panels for $t_d = 2$ s, and lower panels for $t_d = 4$ s. The scanning velocity is the same for all the simulations ($v_{scan} = 10$ arcsec/sec).

3 Imaging techniques for mosaics

3.1 Basic image synthesis

The fundamentals of image synthesis and deconvolution have been treated extensively in the literature. The interested reader is referred to Guilloreau (2000), Briggs, Schwab & Sramek (1999) and Cornwell, Braun & Briggs (1999). Below we describe briefly the imaging and deconvolution processes for a single field observation.

The interferometer measures the visibility function, which is the Fourier transform of the source brightness distribution apodized by the primary beam (power pattern) of the antennas (Eq. 1). Indeed the visibilities are only measured over an ensemble of points $(u_i, v_i), i = 1, n$. Let $S(u, v)$ be the *sampling (or spectral sensitivity) function*. The value of this function is zero for the (u, v) points where the visibility has not been measured ($S(u, v) = 0 \iff \forall (u, v) \neq (u_i, v_i); i = 1, n$). On the other hand, for the (u_i, v_i) points with measured visibilities, $S(u, v)$ contains information on the relative weights of each visibility, usually derived from noise predicted from the system temperature, antenna efficiency, integration time and bandwidth.

In order to synthesize an image of the sky it is clear that one has to compute an inverse Fourier transform. However, taking into account the considerations described above on the partial coverage of the uv plane, the visibility function should be weighted by the function $S(u, v)$. Doing this, one obtains the so called *dirty image* $I_w(l, m)$:

$$I_w(l, m) = \iint S(u, v)V(u, v)e^{2i\pi(ul+vm)}dudv. \quad (10)$$

It is also possible to use an additional function to multiply the sampling function. This is typically done to change the relative weights of high versus low spatial frequencies (long versus short baselines).

In addition, one can define the dirty beam $D_w(x, y)$ as the point spread function:

$$D_w(l, m) = \iint S(u, v)e^{2i\pi(ul+vm)}dudv \quad (11)$$

The process known as *imaging* consist in computing the dirty image and the dirty beam from the measured visibilities and the spectral sensitivity (or sampling) function, possibly multiplied by an additional weighting function. The Fourier Transform of a product of two functions is the convolution of the Fourier Transforms of the functions. Applying this property on Eq. 10 and using Eqs. 1 and 11, the dirty image $I_w(l, m)$ can be written as the convolution product of the sky brightness distribution (apodized by the interferometer primary beam) by the dirty beam:

$$I_w(l, m) = [B(l, m)I(l, m)] * [D_w(l, m)] \quad (12)$$

Which is another form of the *measurement equation*. Therefore, once the dirty beam and the dirty image have been calculated, to derive the astronomically meaningful result, i.e. ideally the sky brightness, a deconvolution is required. Unfortunately, the problem is not straightforward since the dirty beam $D_w(l, m)$ has not a convolutional inverse and the data are noisy. Therefore, we cannot perform an actual deconvolution. Fortunately, several techniques exist to find plausible solutions, that is functions whose convolution with the dirty beam is in agreement with the dirty image (this is what is commonly known as deconvolution in radio astronomy). To better select between the possible plausible solutions additional constrains can be imposed

(e.g. positivity, or user specified finite support). The astronomer must keep in mind that due to the many zeros in the sampling function the solution is not unique and may try to impose additional physical constraints based on his/her knowledge of the source.

3.1.1 Gridding and sampling

In practice, it is convenient to work with FFTs (Fast Fourier Transforms), which implies that the data should be regularly sampled. This is usually done by a convolution with a gridding kernel G and multiplication by a *bed-of-nails* function \mathbb{III} . Therefore, instead of working with S and $V \cdot S$, one works with the following gridded functions (to simplify the notation hereafter we will write \mathbf{l} and \mathbf{u} for the vectors (l, m) and (u, v)):

$$V^g(\mathbf{u}) \equiv [(V(\mathbf{u})S(\mathbf{u})) * G(\mathbf{u})] \frac{1}{\Delta \mathbf{u}} \mathbb{III}\left(\frac{\mathbf{u}}{\Delta \mathbf{u}}\right) \quad (13)$$

and

$$S^g(\mathbf{u}) \equiv [S(\mathbf{u}) * G(\mathbf{u})] \frac{1}{\Delta \mathbf{u}} \mathbb{III}\left(\frac{\mathbf{u}}{\Delta \mathbf{u}}\right) \quad (14)$$

It is important to bear in mind that the gridding and sampling processes are nontrivial operations. First, the sampling spacing $\Delta \mathbf{u}$ must be chosen properly to avoid *aliasing*. Second, it is necessary to probe that one can do the imaging using the gridded functions V^g and S^g and correct for the gridding convolution at the end. Let us apply the imaging process as described above but using the gridded functions. In this case, the dirty image computed with the gridded data is:

$$I_w^g \equiv FT[V^g] = FT[(VS) * G] = \widetilde{VS} \cdot \tilde{G} = I_w \cdot \tilde{G}, \quad (15)$$

while the dirty beam is given by:

$$D_w^g \equiv FT[S^g] = FT[S * G] = \tilde{S} \cdot \tilde{G} = D_w \cdot \tilde{G} \quad (16)$$

Therefore, the dirty image and the dirty beams can be recovered from those computed with the gridded data just dividing by the Fourier transform of the gridding convolution kernel. Using the gridded dirty image and beam, the measurement equation is:

$$\frac{I_w^g}{\tilde{G}} = \frac{D_w^g}{\tilde{G}} * (B \cdot I) \quad (17)$$

3.2 Mosaic imaging as linear combination of individual images

The standard imaging method for SAG mosaics deal with the different mosaic fields independently. The simplest idea is doing a linear combination of CLEANed images, which could be summarized as follows:

- First all the fields should have the same phase center. A shift is applied if this is not the case
- The visibilities measured for each field are Fourier transformed to obtain dirty images

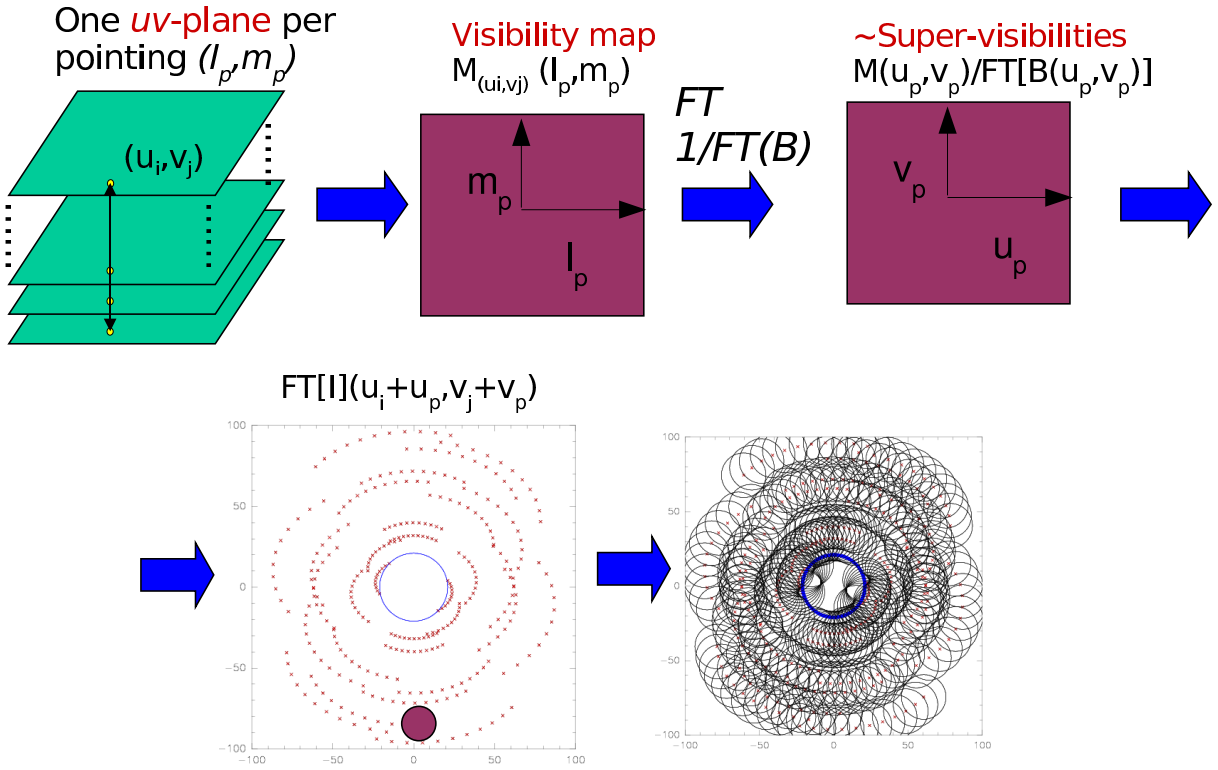


Figure 4: Schema showing the main steps to transform n_{fields} uv planes (one per mosaic field) into one global uv plane using the ER79 scheme. The global uv plane contains all the information on the mosaic and has a very good uv coverage. See text for more details.

- The individual images are deconvolved of the dirty beams (which in principle are different for all the fields)
- A mosaic is done by combination of the deconvolved images

However, this method is just doing a collage of individual images and we do not get any additional information. Alternatively one can invert the two last steps and the method would be as follows:

- First all the fields should have the same phase center. A shift is applied if this is not the case
- The visibilities measured for each field are Fourier converted to obtain dirty images
- The images are combined additively
- A joint deconvolution of the mosaic is done

The two methods are not equivalent since the deconvolution algorithms (CLEAN, MEM) are not linear. The joint deconvolution allows to recover large scale structure that is not present in the individual images of the different mosaic fields (see Cornwell, Holdaway & Uson 1993, Holdaway 1999 and Gueth 2000 for a more detailed description).

3.3 An alternative method to image mosaic data: constructing a global uv -plane using the Ekers & Rots scheme

Another possibility when dealing with mosaics is two construct a global uv -plane containing all the information of the individual fields and to do the imaging process at once. This approach is based on an idea by Ekers & Rots (1979), hereafter ER79 (see also Cornwell 1987, 1888), who suggested that in Eq. 3 one can perform a Fourier transform of $V(\mathbf{u}, \mathbf{l}_p)$ with respect to the position variable \mathbf{l}_p . This operation should be done for a given \mathbf{u}_i that is kept constant. Hereafter, we will define the *visibility map* $M_{\mathbf{u}_i}(\mathbf{l}_p)$ as:

$$M_{\mathbf{u}_i}(\mathbf{l}_p) \equiv V(\mathbf{u}, \mathbf{l}_p)|_{\mathbf{u}=\mathbf{u}_i}. \quad (18)$$

The process is described schematically in Fig. 4. Lets assume that we have observe a mosaic of n_{fields} fields. We will have n_{fields} uv planes. We select a frequency \mathbf{u}_i and we plot the value of the source visibility at this frequency as a function of the position across the source (visibility map). Then one can compute the Fourier transform of the visibility map:

$$\tilde{M}_{\mathbf{u}_i}(\mathbf{u}_p) \equiv \int V(\mathbf{u}_i, \mathbf{l}_p) e^{-i2\pi\mathbf{u}_p\mathbf{l}_p} d\mathbf{l}_p \quad (19)$$

Using Eqs. 3 and 19 we can write:

$$\tilde{M}_{\mathbf{u}_i}(\mathbf{u}_p) = \int \left(\int B(\mathbf{l} - \mathbf{l}_p) I(\mathbf{l}) e^{-i2\pi\mathbf{u}_i\mathbf{l}} d\mathbf{l} \right) e^{-i2\pi\mathbf{u}_p\mathbf{l}_p} d\mathbf{l}_p = \quad (20)$$

$$= \int \left(\int B(\mathbf{l} - \mathbf{l}_p) e^{-i2\pi\mathbf{u}_p\mathbf{l}_p} d\mathbf{l}_p \right) I(\mathbf{l}) e^{-i2\pi\mathbf{u}_i\mathbf{l}} d\mathbf{l} = \quad (21)$$

$$= \int \tilde{B}(\mathbf{u}_p) e^{-i2\pi\mathbf{u}_p\mathbf{l}} I(\mathbf{l}) e^{-i2\pi\mathbf{u}_i\mathbf{l}} d\mathbf{l} = \quad (22)$$

$$= \tilde{B}(\mathbf{u}_p) \int I(\mathbf{l}) e^{-i2\pi(\mathbf{u}_i + \mathbf{u}_p)\mathbf{l}} d\mathbf{l} = \quad (23)$$

$$= \tilde{B}(\mathbf{u}_p) \tilde{I}(\mathbf{u}_i + \mathbf{u}_p) \quad (24)$$

Therefore, there is a simple relation linking the Fourier transform of the visibility map for frequency \mathbf{u}_i and the Fourier transform of the source brightness distribution (without apodisation by the primary beam) around the point \mathbf{u}_i :

$$\tilde{M}_{\mathbf{u}_i}(\mathbf{u}_p) = \tilde{B}(\mathbf{u}_p) \tilde{I}(\mathbf{u}_i + \mathbf{u}_p) \quad (25)$$

Hereafter, we will define the *supervisibility* function V_S as the Fourier transform of the visibility maps divided by the Fourier transform of the primary beam:

$$V_{S_{\mathbf{u}_i}}(\mathbf{u}_p) \equiv \tilde{M}_{\mathbf{u}_i}(\mathbf{u}_p) / \tilde{B}(\mathbf{u}_p), \quad (26)$$

for $|\mathbf{u}_p| < D/\lambda$ (where $\tilde{B}(\mathbf{u}_p) \neq 0$). Therefore,

$$\tilde{I}(\mathbf{u}_i + \mathbf{u}_p) = V_{S_{\mathbf{u}_i}}(\mathbf{u}_p) \quad (27)$$

Therefore, the *supervisibility* function are samples of the FT of the source brightness distribution. Equation 27 implies that, from the measurements done at the point \mathbf{u}_i for every field, it is possible to construct a **super- uv plane** or **global- uv plane** summarizing the information of all the individual uv planes in the form of samples of the *true* visibilities of the

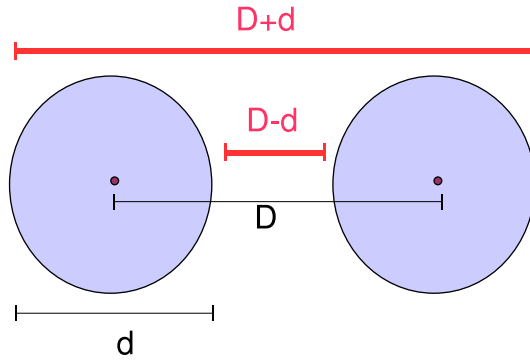


Figure 5: If the distance between two antennas of diameter d is D , the antenna pair is sampling frequencies corresponding to all the spacings between $D - d$ and $D + d$.

source within a disk of radius D/λ centered in \mathbf{u}_i . This is represented in the lower left panel of Fig. 4. Repeating the process for all the measured uv points one get a global uv plane for the mosaic with a very good coverage (lower right panel of Fig. 4). Of course, in order to conserve all the information, the observed region must be sampled at a rate higher than the Nyquist sampling rate, i.e., the mosaic fields should be spaced by less than $D/(2\lambda)$ (half the FWHM of the primary beam).

The intuitive idea behind the ER79 scheme is that an antenna pair is not only sampling the spatial frequencies corresponding to the distance D from one antenna to the other. If the diameter of the antennas is d they are indeed sampling frequencies corresponding to baselines from $D - d$ to $D + d$ (Fig. 5). Performing Fourier Transforms of the visibility maps with respect to the pointing coordinates we analyze how a given visibility change from one point of the source to another point. Thus, the Fourier transform of the visibility map gives *explicitly* the value of the visibility for all the frequencies corresponding to baselines from $D - d$ to $D + d$ for each antenna pair.

3.3.1 The Ekers & Rots scheme versus real interferometers

For simplicity, the ER79 scheme has been presented above using continuous functions and Fourier transforms and assuming that one can measure the visibility function at the same (u, v) point for all the mosaic fields. The actual data will differ from the idealized ER79 theory in a number of points.

- The actual uv coverage of an interferometer is limited: in a real experiment we only get (noisy) samples of the visibility function. This imposes the introduction of a sensitivity function to weight the visibilities when doing Fourier transforms. In addition, for computational efficiency one would like to perform discrete Fast Fourier Transforms (FFTs) and therefore one should grid the data. Therefore, the global process will be something like those shown in Fig. 6 instead of the simplistic representation in Fig. 4. The gridding process (interpolation and sampling) introduces numerical effects take one should be able to correct in later stages of the data processing. Gridding the data in the uv plane is done in standard imaging techniques, and it is well known that one can correct for its numerical effects (see Sect. 3.1). However, one should be sure that in the case of the much more

complicate and longer data processing in the ER79 context, one will be able to correct for the gridding at some stage.

- In the case of ER79 an additional gridding process can be required in the $\mathbf{l}_p, \mathbf{m}_p$ plane (second row in Fig. 6). In this case, it is also needed to ensure that one can correct later on for the numerical effects introduced, which is not trivial. However, imposing some constraints on the observing mode (mosaicing using cartesian grids) would allow to have a natural gridding in the $\mathbf{l}_p, \mathbf{m}_p$ plane.
- ER79 consider that we can actually measure the visibility function at the same (u, v) point for all the mosaic fields. In contrast, due to the earth rotation this is not possible since as time goes by, the interferometer measures the visibility function at different points along a uv track. The possible observational constraints to avoid this will be very hard from the scheduling point of view (performing the observations of the different fields in different days), will rule out the possibility of doing the mosaics in OTF mode and the noise could significantly change across the mosaic. Therefore, the only possible way of dealing with this is limiting the shift of the uv points in the uv plane by limiting the mosaic size and the observing time for a full coverage of the mosaic (we have analyzed these constraints in Sect. 4).

3.4 Comparison of the two methods

Doing a linear combination of images and a joint deconvolution allows to recover some spatial frequencies that are not accessible in the single field observations (see for instance Helfer et al. 2002 and references therein). Indeed, the deconvolution algorithm works to find a structure on the sky that is consistent with all the sampled visibility data but that also provides a more plausible and robust model of the unsampled visibility data (see for instance Cornwel, Braun & Briggs 1999). The deconvolution not only interpolates between sampled visibility data, it can also effectively extrapolate to shorter spatial frequencies that the interferometer actually measured.

On the other hand, the ER79 scheme is an elegant way of dealing with mosaic data as a whole. It uses all the information contained in the dataset since it analyzes not only the visibilities of each field but also how the visibilities change from one field to another. The pointing axes open new ways of data edition and processing. In particular, they allow to recover explicitly the visibility for all the frequencies from $D-d$ to $D+d$ for each antenna pair. The global or super- uv -plane contains all the information of the mosaic. At the end only a Fourier Transform is needed to obtain a wide field image containing all the possible spatial frequencies. Therefore, an Ekers & Rots algorithm is a potentially very powerful method to deal with mosaic data, which allows to recover explicitly the source visibility for spacings between $D-d$ and $D+d$ for each antenna pair instead of relying only on the interpolation performed by the deconvolution algorithms.

Finally, it is important to remark, that taking data in OTF mode does not imply necessarily that one has to perform the imaging by constructing a global uv -plane. On the one hand, the ER79 scheme can also be used to image pointed stop-and-go mosaic data provided that the fields are spaced by less than the Nyquist critical spacing. On the other hand, data taken in OTF observing mode can be imaged using standard stop-and-go mosaics techniques, i.e., computing a dirty image per OTF dump and doing a linear combination of those dirty images before applying a joint deconvolution.

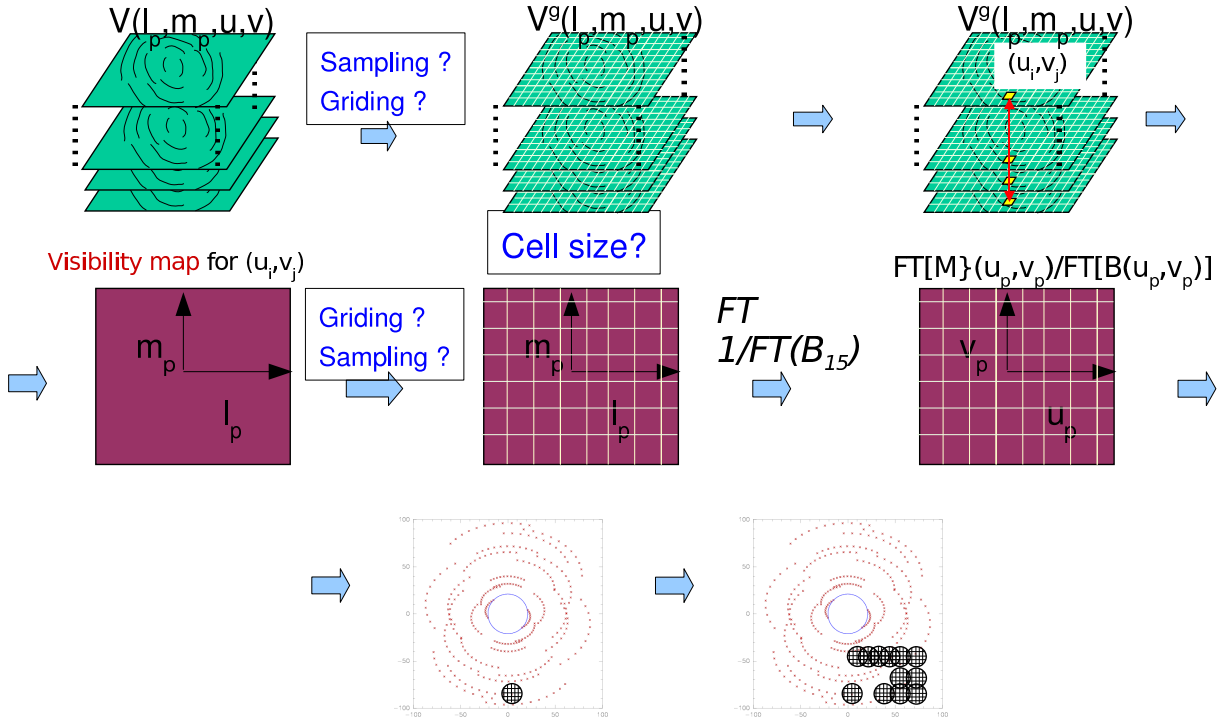


Figure 6: Schema of the different steps needed to implement an imaging algorithm based in ER79 taking into account the incomplete uv coverage and an additional gridding step in the (l_p, m_p) plane. The questions in blue remark that gridding and sampling are not-trivial operations and that one should be able to correct for their numerical effects at later stages of the processing. A critical point it is also to use an adapted cell size (see text).

4 Mosaic size and observing time limitations for OTF observations

Before discussing several possible ways to do the image synthesis with OTF data, it is interesting to analyze different limitations that can impose constraints on the total observing time and the mosaic size. Ideally, to use the ER79 scheme, one should have a measurement of the source visibility for the same uv point for all the fields/dumps. Although this is not possible due to Earth rotation, at least one must impose a reasonable limit to the distance between the uv points sampled for each field/dump. In addition, size and time constraints to the OTF maps should be imposed to avoid sensitivity losses due to decorrelation when using a constant phase tracking center for an OTF scan.

4.1 Earth rotation: different uv coverages for the different fields/integrations

Due to the Earth rotation, the spatial frequency sampled by a given antenna pair change along a uv -track. This has two effects:

1. Each visibility measurement is indeed an average of the source visibility for the frequencies sampled by an antenna pair along the integration or dumping time. The effect on the images is an azimuthal smearing, limiting the smearing to a small angular fraction of the synthesized beam it is possible to obtain upper limits field of view (see Guilloteau 2000,

Cotton 1999, Bridle & Schwab 1999 or Perley 1999). Since those fields of view are larger than the primary beam of the ALMA antennas, this is not really a limitation.

2. When observing sequentially the different fields of a mosaic, the interferometer does not measure the visibility of the source at the same (u, v) point for all the mosaic fields. However, the ER79 scheme relies on the assumption that one has actually measured the visibility at the same spatial frequency for all the fields.

This effect has been discussed by Holdaway & Foster (1994) in the context of mosaics with a high number of fields (250-16000) and in terms of the differences in the synthesized beam for the different mosaic fields. Indeed, if the uv coverage of different pointings in a mosaic is significantly different, the synthesized beam change over the mosaic image. This makes the interpretation of the combined image more difficult, for instance, the deconvolution errors will be different across the image. If the uv coverage of each pointing cannot be assumed to be identical, the linear mosaic algorithm cannot be used. Instead one should use a non-linear algorithm taking into account one synthesized beam per pointing. On the contrary, one can set limits to the differences in the uv coverage of the different fields of a mosaic to simplify the data processing and analysis. Among the possibilities to ensure that the uv coverages are similar for all the fields there are:

- To put strong observational constraints such as scheduling mosaics in blocks of the same LST over several days and for a small hour angle or using snapshots symmetrically spaced in hour angle.
- Reducing the integration time per mosaic field. For instance if the typical settle down times for an antennas is 1 sec, it will not be efficient to spend less than 3 sec on each pointing when doing SAG mosaics. In contrast, the OTF observing mode can be used to accelerate the data acquisition.

Holdaway & Foster (1994) used a compact strawman configuration with maximum baselines of 95 meters and they found that to have normalized beam area differences of less than 1%, the time used to cover the full mosaic should be less than 4 minutes. The actual size of the mosaic depends on the scanning velocity and the dumping time. For instance, a dumping time of 0.96 sec allows to observe a $4.3' \times 4.3'$ mosaic (which implies a scanning velocity of ~ 16.8 arcsec/sec) while a dumping time of 0.24 sec will allow a mosaic of $8.6' \times 8.6'$ (with a scanning velocity of ~ 67 arcsec/sec). If normalized beam areas differences up to 5% are acceptable, the maximum time to cover the full mosaic increases to 15 minutes, allowing longer dumping times or larger mosaic sizes.

In this memo, we discuss the shift of the uv points sampled for each mosaic field/dump in the context of OTF mosaics and an imaging process based on the ER79 scheme. In this scheme, one should construct a visibility map for each spatial frequency measured and apply a Fourier transform. To do this, ideally the interferometer should measure the source visibility for all the fields at the same spatial frequency. This is not possible, however one can impose a time limit for observing the whole mosaic in a way that the uv point sampled for the last field to be observed is not too far from the uv point sampled for the first observed field.

What does "too far" mean in this context? If the size of the map is $\Delta l \times \Delta m$, the smaller frequencies that we can sample in the uv plane are $\frac{1}{\Delta l}$ and $\frac{1}{\Delta m}$. If we sample the uv plane at intervals $\Delta u = \frac{1}{2\Delta l}$ and $\Delta v = \frac{1}{2\Delta m}$ we can recover all the information. When imaging large

Table 1: Observing time (t_{cover}) for one coverage of the OTF mosaic and map size as a function of the scanning velocity (v_{scan}). The calculations have been done for PdBI observations of a source with a declination of 30 deg and a largest baseline of 92 m (D configuration)

v_{scan} arcsec/sec	t_{cover} min	map linear size arcmin
0.5	18	1.9
1	14	2.4
5	8.8	4
10	7	5
20	5.4	6.5
40	4.4	8
60	3.8	9.1

fields it is recommendable to have, for every baseline and pointing, a visibility measurement within a region of size $\Delta u \times \Delta v$. In this case, we can assume that we have indeed sampled the same spatial frequency for all the fields and we can compute the Fourier transform of the visibility map.

Taking into account, the relation linking the map size ($\Delta l \times \Delta m$) and the size of the corresponding cells in the uv -plane ($\Delta u \times \Delta v$), it is possible to derive consistent mosaic sizes and maximum observing time for a full coverage of the mosaic as follows.

- Let assume a scanning velocity v_{scan} and an observing time t_{cover} for one coverage of the full mosaic. Given these times and scanning velocity, it is easy to calculate the size of the mosaic that one can observe. Let us assume that the size is $\Delta l \times \Delta m$. In principle, the longer the time t_{cover} , the larger the region ($\Delta l \times \Delta m$) that one can observe.
- However, as mentioned above, due to the Earth rotation during the time t_{cover} , the uv point sampled for the last field of the mosaic is shifted with respect to the uv point sampled for the first mosaic field. One should take care that the distance between those uv points is smaller than the characteristic size in the uv plane ($\sqrt{(\frac{1}{\Delta l})^2 + (\frac{1}{\Delta m})^2}$) to image the mosaic. This criterium gives an upper limit to the time t_{cover} and the mosaic size $\Delta l \times \Delta m$.

For instance, Table 1 gives time and mosaic size limits for PdBI observations of a source with a declination of 30 deg in D configuration (largest baseline of 92 m, similar to the largest baselines in the Holdaway & Foster 1994). A comparison of our results with those of Holdaway & Foster (1994) shows that our criterion is similar, but slightly less constraining, to their "normalized beam areas difference of less than 1%".

The dumping time The mosaic size depends only of the total time and the scanning velocity. The effect of the dumping time is just to obtain a different sampling, that is to decompose the mosaic in a different number of fields. The maximum scanning velocity and the minimum dumping times are limited by hardware and software of the acquisition system of the interferometer. For instance, for PdBI, the maximum scanning velocity limit for the antennas is ~ 60 arcsec/sec (the specifications for ALMA are 3 arcmin/sec to conserve a pointing accuracy of 1 arcsec). On the other hand, the minimum integration time in continuum mode is 1 sec.

With the improvements done in the data acquisition system in the framework of the FP6 program "Enhancement of ALMA", the minimum dumping time in spectral mode has also been reduced to ~ 1 s.

In addition, the dumping time and the scanning velocity are linked in order to have a correct sampling. For instance, to have about four integrations per FWHM with the PdBI at 3 mm one gets $t_{dump} \times v_{scan} = \text{FWHM}/4$ or: $v_{scan} \sim 10''/t_{dump}$. With a minimum t_{dump} of 1 sec, the maximum scanning velocity will be $10''/\text{sec}$ and therefore the maximum mosaic size $5'$ (and the total observing time for a full coverage is 7 minutes). It is interesting to remark, that it is needed to observe a calibrator every 20 minutes. Thus, it will be possible to do 2 or 3 OTF mosaics in between each calibrator observation.

4.2 Fringe tracking: coherence loss when using a fixed phase-center

D'Addario & Emerson (2000) have discussed how to accomplish the necessary phase and delay tracking during an OTF observation. In principle, there are three possibilities:

1. Track a fixed point on the sky during each integration, typically the point to which the antenna beams point at the middle of that integrating time, which is the center of the effective beam (Fig. 2).
2. Track the center of the antenna beams, which means that the phase/delay center on the sky moves continuously with the beams.
3. Track a fixed point on the sky for the full duration of an OTF scan, and switch to a new phase/delay center only between scans, when the antenna is off source and no integration is occurring.

Tracking a different point for each integration requires that the phase change discontinuously (or nearly so), and that the changes be synchronized with the end/beginning of a correlator integration. Both of these things are technically difficult. Continuous tracking of the beam center is possible, but it results in a smearing of the visibility function during the integrating time and may be difficult to account for in the imaging process. Therefore, D'Addario & Emerson (2000) proposed to track a fixed point on the sky throughout the OTF scans. This is easy, but at the ends of the scan, when the beam is offset from the phase center, there is a loss of sensitivity because the fringe frequency is not correct. They have estimated the decorrelation at the end of an OTF scan of length $2NB$ arcsec (where B is the primary beam WHM and assuming that the phase center is located in the middle of the scan). Setting a decorrelation limit of 2%, the maximum value of N as a function of the dumping time is:

$$N < \frac{0.346}{1.2 \pi \Omega} \frac{d}{D} \frac{1}{t_{dump}} \quad (28)$$

Taking $D=1$ km and $d=12$ m one gets a maximum N of 15 for $t_{dump} = 1$ sec, which implies an scan length of 11 arcmin. Assuming that there are four integrations per primary beam, the time needed to observe a scan is $t_{scan} = 8Nt_{dump}$, that is 120 sec. Of course, if the dumping time is shorter, the scan length can be larger by the same factor, keeping t_{scan} constant.

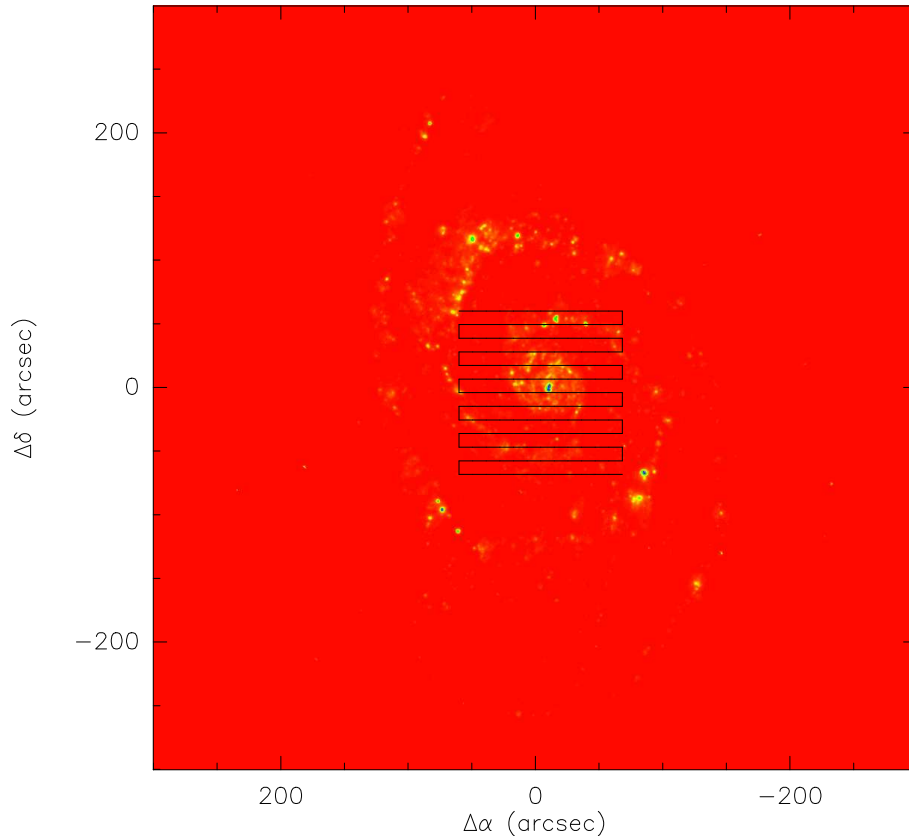


Figure 7: Scanning pattern for a simulated OTF observation of a scaled version of an $H\alpha$ image of M51.

5 Imaging techniques for OTF mosaics

5.1 One dirty image per dump, linear combination and joint deconvolution

As we have shown in Sect. 2, OTF mosaicing is equivalent to stop-and-go mosaicing with an effective beam given by Eq. 6. We have also discussed in Sect. 2 that when observing OTF, one wants to sample the source at a sampling rate better than Nyquist, integrating several times per FWHM of the primary beam power pattern. In this case the effective beam for OTF observations is very similar to the primary beam of the antennas. Therefore, as a first approximation it is logical to image OTF data as a classical stop-and-go mosaic where each OTF integration corresponds to an independent field.

Taking into account the previous comments, we have developed a simulator of OTF interferometric observations on the base of the IRAM ALMA simulator (Pety, Gueth & Guilloteau 2001c). For given array configuration, source declination, map size, scanning velocity and dumping time, the OTF simulator computes the visibility of an input sky brightness distribution. A more detailed description can be found in Rodriguez-Fernandez, Gueth & Pety (2009). The OTF observation is simulated on a Cartesian grid following a zigzag pattern at an arbitrary angle (not necessarily in R.A. or Declination). The row separation is half the FWHM of the primary beam at the frequency of the observations. For instance, we have done simulations of OTF observations of a scaled version of a $H\alpha$ image of M51. The array used in this simulations

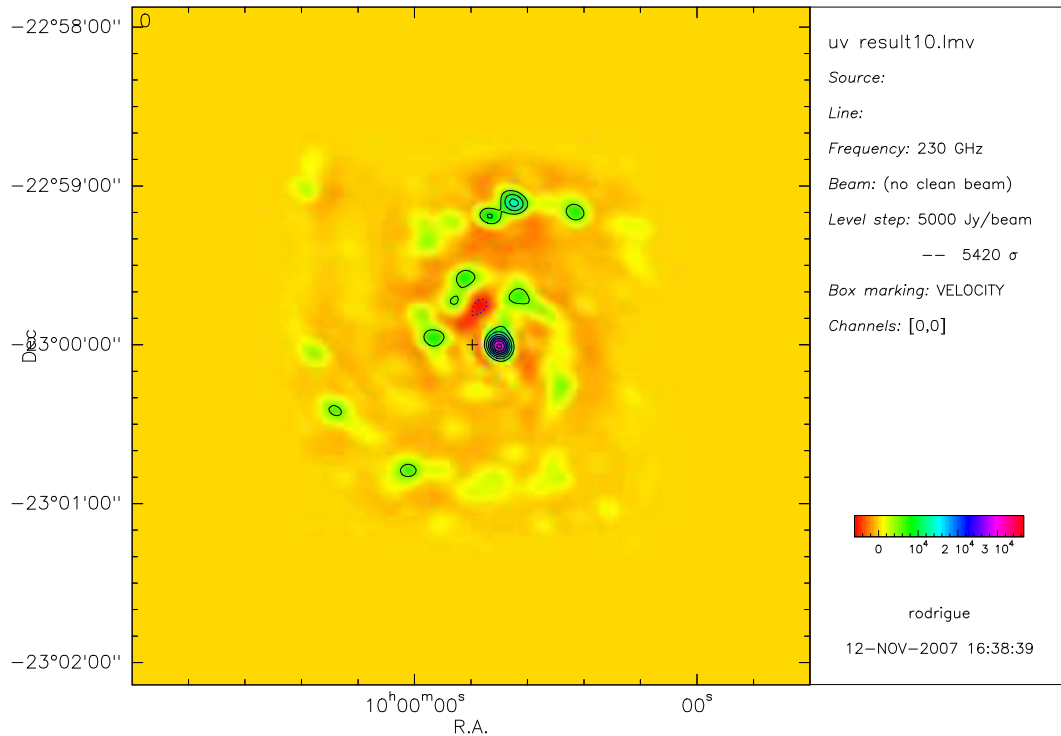


Figure 8: Dirty image of the OTF mosaic computed as a linear combination of the dirty images of the individual fields.

is ACA and the assumed frequency is 230 GHz. Figure 5.1 shows the OTF pattern for a map size of $2' \times 2'$ scanned in with a velocity of 1 arcsec/sec and a dumping time of 3 sec, which give 13×41 dumps per OTF map. The total observing time is 5 hours, which allows to do 11 OTF maps (the simulations does not take into account observations of the calibrators).

The image synthesis has been performed by computing independent dirty images and combining them linearly to produce a mosaic dirty image, which is shown in Fig. 8. Finally the mosaic dirty image has been deconvolved using CLEAN. The CLEANed image is shown in Fig. 9. The conclusion is that the OTF mosaics can actually be imaged and deconvolved by linear combination of dirty images and a joint deconvolution.

5.2 Constructing a global uv-plane and dirty image

The uv coverage of an interferometer array will always be partial (or at least inhomogeneous in the case of ALMA), requiring the introduction of a sampling or weighting function $S(\mathbf{u})$. In addition, to be able to use Fast Fourier Transforms one should resample the data on a regular grid. This is usually done by convolution with a gridding kernel $G(\mathbf{u})$ and sampling with a bed-of-nails function $\text{III}(\mathbf{u})$.

In contrast, regarding the \mathbf{l}_p plane one can assume, as a first approximation, that:

- The data are naturally gridded in the \mathbf{l}_p plane by the observational procedure (i.e. the mosaic has been done in a Cartesian grid) allowing the use of FFTs without any resampling.
- The \mathbf{l}_p coverage is complete (i.e. the interferometer has measured the visibility function

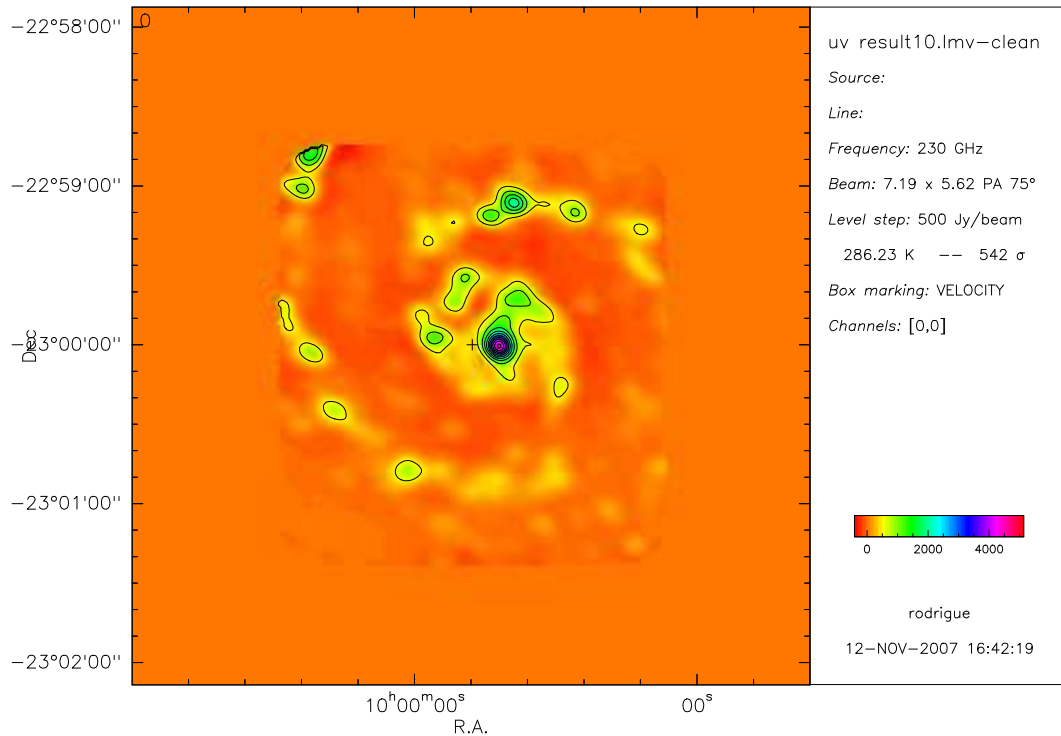


Figure 9: Deconvolved OTF mosaic data using CLEAN

in all the uv points sampled by a given array configuration for all the fields/dumps), therefore there is no need of introducing a sampling function in this plane.

Taking into account the standard method of image synthesis (Sect. 3.1) and the particularities of the ER79 method to image mosaic data (Sect. 3.3), it is clear that there could be two possible options to start the data processing. One can start by gridding the individual uv planes, or alternatively, one can start by computing Fourier transforms with respect to the pointing coordinates. This would be possible if the Fourier transform with respect to \mathbf{l}_p and convolution by $G(\mathbf{u})$ commute. If the resampled visibility function is:

$$V^g(\mathbf{l}_p, \mathbf{u}) = [V(\mathbf{l}_p, \mathbf{u}) * G(\mathbf{u})] \frac{1}{\Delta \mathbf{u}} \text{III}\left(\frac{\mathbf{u}}{\Delta \mathbf{u}}\right), \quad (29)$$

and one performs a $\text{FT}_{\mathbf{l}_p}$, it is possible to show that indeed those operations commute:

$$\text{FT}_{\mathbf{l}_p}[V^g(\mathbf{l}_p, \mathbf{u})] = \text{FT}_{\mathbf{l}_p}\left\{[V(\mathbf{l}_p, \mathbf{u}) * G(\mathbf{u})] \frac{1}{\Delta \mathbf{u}} \text{III}\left(\frac{\mathbf{u}}{\Delta \mathbf{u}}\right)\right\} = \quad (30)$$

$$= [\text{FT}_{\mathbf{l}_p}\{V(\mathbf{l}_p, \mathbf{u})\} * G(\mathbf{u})] \frac{1}{\Delta \mathbf{u}} \text{III}\left(\frac{\mathbf{u}}{\Delta \mathbf{u}}\right) \quad (31)$$

$$(32)$$

Therefore, in principle one can chose to resample the data in the uv plane and Fourier Transform with respect to the pointing coordinates or to Fourier Transform with respect to the pointing coordinates and afterwards gridding in the uv-plane.

5.2.1 Beginning by Fourier Transforming the visibility maps

In the following, we describe how the image synthesis can be done if one begins the process by Fourier transforming the data with respect to the \mathbf{l}_p coordinates. As already mentioned, as a first approximation we will consider that the data are naturally gridded in the \mathbf{l}_p plane and that there are no gaps.

The first step will be constructing *visibility maps* for each \mathbf{u}_i point sampled by the interferometer. The visibility map $M_{\mathbf{u}_i}(\mathbf{l}_p)$ gives the visibility at frequency \mathbf{u}_i as a function of the pointing coordinate \mathbf{l}_p :

$$M_{\mathbf{u}_i}(\mathbf{l}_p) \equiv V(\mathbf{l}_p, \mathbf{u})|_{\mathbf{u}=\mathbf{u}_i} \quad (33)$$

Afterwards, for each \mathbf{u} point, one should Fourier transform the visibility map with respect \mathbf{l}_p and divide by the FT of the primary beam (applying a truncation at some level to avoid divergences) to compute supervisibilities at points $\mathbf{u}_i + \mathbf{u}_p$.

$$V_S(\mathbf{u}) = V_S(\mathbf{u}_i + \mathbf{u}_p) = \frac{\tilde{M}_{\mathbf{u}_i}(\mathbf{u}_p)}{\tilde{B}(\mathbf{u}_p)} \quad (34)$$

The natural weights of a visibility map will be approximately constant and they will remain approximately constant after the Fourier transform. In contrast, the weights will decrease towards the edges after division by the Fourier Transform of the primary beam pattern. Therefore, the weight distribution for the supervisibilities will be given by the square of the primary beam pattern. The weights will be assigned following this distribution and conserving the total weight (in a similar way as it is done in the pseudovisibilities calculations to include the short-spacings information, see Rodríguez-Fernández, Pety & Gueth 2008).

Repeating this process for all the \mathbf{u}_i points sampled by the interferometer one will end with a global \mathbf{u} plane containing all the information of the mosaic where each original \mathbf{u}_i point is replaced by a “cloud” of points, each with an associated weight. The actual imaging of this dataset can be performed resampling the data to a Cartesian grid (by convolution with a gridding kernel and sampling with a bed-of-nails function), computing a dirty image and beam, and applying a correction for the gridding convolution as described in Sect. 3.1. In summary, in this case, the actual imaging will be exactly the same that is used to image a single field. The difference will be all the *pre-processing* applied to construct the global \mathbf{u} plane. This method has been applied by Wright (1996) to BIMA data, for which it seems to perform worse than other methods based on a classical field-by-field approach to imaging.

When the visibility maps are not naturally gridded Now let us assume that the visibility maps are not naturally gridded because they have been observed in a Cartesian grid but there are gaps for some \mathbf{l}_p 's or simply because the scanning pattern was not a Cartesian grid and the data have not been regridded. In this case one should introduce a sampling function $S_l(\mathbf{l}_p)$ and perform a gridding, i.e., interpolation by convolution with a gridding kernel $G_l(\mathbf{l}_p)$ and sampling by multiplication by a bed-of-nails function. Thus one will work with the gridded versions of $M_{\mathbf{u}_i}(\mathbf{l}_p)$ and $S_l(\mathbf{l}_p)$: $M_{\mathbf{u}_i}^{gr}(\mathbf{l}_p)$ and $S_l^{gr}(\mathbf{l}_p)$, respectively. These functions are defined mathematically as:

$$M_{\mathbf{u}_i}^{gr}(\mathbf{l}_p) \equiv [M_{\mathbf{u}_i}(\mathbf{l}_p)S_l(\mathbf{l}_p)] * G_l(\mathbf{l}_p) \quad (35)$$

and

$$S_l^{gl}(\mathbf{l}_p) \equiv S_l(\mathbf{l}_p) * G_l(\mathbf{l}_p) \quad (36)$$

Following the processing in the ER79 context one should Fourier transform the visibility map:

$$\tilde{M}_{\mathbf{u}_i}^{gl}(\mathbf{u}_p) \equiv \text{FT}_{\mathbf{l}_p}[M_{\mathbf{u}_i}^{gl}(\mathbf{l}_p)] = \text{FT}_{\mathbf{l}_p}[(M_{\mathbf{u}_i}(\mathbf{l}_p)S_l(\mathbf{l}_p)) * G_l(\mathbf{l}_p)] \quad (37)$$

and therefore:

$$\tilde{M}_{\mathbf{u}_i}^{gl}(\mathbf{u}_p) = (\tilde{M}_{\mathbf{u}_i} * \tilde{S}_l) \cdot \tilde{G}_l \quad (38)$$

or

$$\frac{\tilde{M}_{\mathbf{u}_i}^{gl}}{\tilde{G}_l} = \tilde{M}_{\mathbf{u}_i} * \tilde{S}_l \quad (39)$$

but since

$$\tilde{S}_l^{gl} = \tilde{S}_l * \tilde{G}_l \quad (40)$$

one gets

$$\frac{\tilde{M}_{\mathbf{u}_i}^{gl}}{\tilde{G}_l} = \tilde{M}_{\mathbf{u}_i} * \frac{\tilde{S}_l^{gl}}{\tilde{G}_l} \quad (41)$$

Therefore, as in classical image synthesis, one can work with the gridded versions of M and S_l and correct for the effects of the gridding convolution dividing by the Fourier transform of the gridding kernel.

However, there is still an important difficulty: to get the function \tilde{M} , it is necessary to perform a deconvolution. It is not obvious how to do such a deconvolution in the \mathbf{u}_p space. First, the point spread function (\tilde{S}_l) is very different from the dirty beam in classical imaging. Second, the visibility maps are computed with individual measurements of visibilities and short integration times, which means that the signal to noise ratio is low. Therefore, it is highly recommendable to observe OTF mosaics along a Cartesian grid and avoid gaps in the visibility map. For an instrument like ALMA, with a very good coverage of the uv -plane it could be possible just to flag out and not to process the visibility maps that have gaps.

5.2.2 Beginning by gridding the independent uv planes

The second possibility to do the image syntheses of mosaicing data will be to begin by gridding the individual uv planes corresponding to each mosaic field/dump and to apply the ER79 scheme to \mathbf{u} cells instead of \mathbf{u} points. Thus, instead of the visibility function $V(\mathbf{l}_p, \mathbf{u})$ and the sampling function $S_{\mathbf{u}}(\mathbf{u})$ one shall work with the gridded versions $V^{gu}(\mathbf{l}_p, \mathbf{u})$ and $S_{\mathbf{u}}^{gu}(\mathbf{u})$ defined as:

$$V^{gu}(\mathbf{l}_p, \mathbf{u}) \equiv [V(\mathbf{l}_p, \mathbf{u})S_{\mathbf{u}}(\mathbf{u})] * G_{\mathbf{u}}(\mathbf{u}) \quad (42)$$

and

$$S_{\mathbf{u}}^{gu}(\mathbf{u}) \equiv S_{\mathbf{u}}(\mathbf{u}) * G_{\mathbf{u}}(\mathbf{u}) \quad (43)$$

In this case the *visibility map for the cell \mathbf{u}_i* is:

$$M_{\mathbf{u}_i}^{g_u}(\mathbf{l}_p) \equiv V^{g_u}(\mathbf{l}_p, \mathbf{u})|_{\mathbf{u}=\mathbf{u}_i}, \quad (44)$$

where the superscript g_u indicate that the visibility map has been defined from data gridded in the \mathbf{u} plane. One can Fourier transform the visibility map w.r.t. \mathbf{l}_p and divide by the FT of the primary beam to compute the super-visibility function around \mathbf{u}_i :

$$V_{S_i}^{g_u}(\mathbf{u}) = V_{S_i}^{g_u}(\mathbf{u}_i + \mathbf{u}_p) = \frac{\tilde{M}_{\mathbf{u}_i}^{g_u}(\mathbf{u}_p)}{\tilde{B}(\mathbf{u}_p)}, \quad (45)$$

where the subscript i of $V_{S_i}^{g_u}(\mathbf{u})$ stands for the fact that the same \mathbf{u} cell can be sampled by different combinations of \mathbf{u}_i 's and \mathbf{u}_p 's. Therefore, in general there are several estimations for the value of the super-visibility function at the cell \mathbf{u} , each with an associated weight, as described in Sect. 5.2.1. In order to compute the actual global uv plane and a unique super-visibility function ($V_S^{g_u}(\mathbf{u}_j)$) it is necessary to compute a weighted mean.

$$V_S^{g_u}(\mathbf{u}_j) = \frac{\sum \omega_{V_{S_i}} V_{S_i}^{g_u}(\mathbf{u}_j)}{\sum \omega_{V_{S_i}}} \quad (46)$$

where the sum is over all the \mathbf{u}_i 's and \mathbf{u}_p 's with $\mathbf{u}_j = \mathbf{u}_i + \mathbf{u}_p$ and the weights $\omega_{V_{S_i}}$ are a function of \mathbf{u}_i and \mathbf{u}_p . Since the different estimations of the value of the function $V_{S_i}^{g_u}$ at the cell \mathbf{u}_j can be considered as independent variables, the weight associated with the function $V_{S_i}^{g_u}$ for the cell \mathbf{u}_j is $W^{g_u}(\mathbf{u}_j) = \sum \omega_{V_{S_i}}(\mathbf{u}_i + \mathbf{u}_p)$

Taking into account Eq. 45, the relation linking the weights of $V_{S_i}^{g_u}(\mathbf{u}_j)$ and $\tilde{M}_{\mathbf{u}_i}^{g_u}(\mathbf{u}_p)$ is:

$$\omega_{V_{S_i}} = \omega_{\tilde{M}_{\mathbf{u}_i}} \tilde{B}^2 \quad (47)$$

$$(48)$$

thus substituting Eq. 45 and Eq. 47 into Eq. 46 one gets:

$$V_S^{g_u}(\mathbf{u}_j) = \frac{\sum \omega_{\tilde{M}_{\mathbf{u}_i}} \tilde{B} \tilde{M}_{\mathbf{u}_i}^{g_u}}{\sum \omega_{\tilde{M}_{\mathbf{u}_i}} \tilde{B}^2} \quad (49)$$

Therefore, we have the global supervisibility function $V_S^{g_u}$, already gridded, and the associated weights W^{g_u} . To get an image one should compute a Fourier transform with respect to \mathbf{u} of the visibility function weighted by W^{g_u} , that is:

$$I(l) = \text{FT}_{\mathbf{u}}[V_S^{g_u}(\mathbf{u})W^{g_u}(\mathbf{u})] = \text{FT}_{\mathbf{u}}[V_S^{g_u}(\mathbf{u})] * \text{FT}_{\mathbf{u}}[W^{g_u}(\mathbf{u})] \quad (50)$$

Therefore, one can compute a dirty image $\text{FT}_{\mathbf{u}}[V_S^{g_u}(\mathbf{u})]$ and a dirty beam $\text{FT}_{\mathbf{u}}[W^{g_u}(\mathbf{u})]$ and afterward, perform a deconvolution. However, the super-index g_u remind us that we have not been working with the original data but with a gridded version. Thus one should try to correct for the convolution with the gridding kernel as it is done in the standard imaging described in Sect. 3.1.

Is it possible to correct for the effects of the gridding convolution? The central idea is that a convolution with a function G in the \mathbf{u} plane is a product by \tilde{G} in the image plane. In the following we will try to develop $\text{FT}_{\mathbf{u}}[V_S^{gu}(\mathbf{u})]$.

$$\text{FT}_{\mathbf{u}}[V_S^{gu}(\mathbf{u})] = \text{FT}_{\mathbf{u}} \left[\sum \frac{\omega_{V_{S_i}}(\mathbf{u}_i + \mathbf{u}_p)}{\sum \omega_{V_{S_i}}(\mathbf{u}_i + \mathbf{u}_p)} V_{S_i}^{gu}(\mathbf{u}_i + \mathbf{u}_p) \right] = \quad (51)$$

$$= \sum \left[\text{FT}_{\mathbf{u}} \left[\frac{\omega_{V_{S_i}}(\mathbf{u}_i + \mathbf{u}_p)}{\sum \omega_{V_{S_i}}(\mathbf{u}_i + \mathbf{u}_p)} \right] * \text{FT}_{\mathbf{u}} [V_{S_i}^{gu}(\mathbf{u}_i + \mathbf{u}_p)] \right] \quad (52)$$

where the sum is over all the \mathbf{u}_i 's and \mathbf{u}_p 's with $\mathbf{u} = \mathbf{u}_i + \mathbf{u}_p$. Now, let us consider the term $\text{FT}_{\mathbf{u}} [V_{S_i}^{gu}(\mathbf{u}_i + \mathbf{u}_p)]$, but first let us remark that taking into account the relation linking \mathbf{u} and \mathbf{u}_p , the operator $\text{FT}_{\mathbf{u}}[\cdot]$ transforms into:

$$\text{FT}_{\mathbf{u}}[\cdot] = e^{-i2\pi\mathbf{u}_i l} \text{FT}_{\mathbf{u}_p}[\cdot] \quad (53)$$

Therefore, with this equation and Eq. 47 one gets:

$$\text{FT}_{\mathbf{u}}[V_{S_i}^{gu}(\mathbf{u}_i + \mathbf{u}_p)] = e^{-i2\pi\mathbf{u}_i l} \text{FT}_{\mathbf{u}_p} \left[\frac{\tilde{M}_{\mathbf{u}_i}^{gu}(\mathbf{u}_p)}{\tilde{B}(\mathbf{u}_p)} \right] = \quad (54)$$

$$= e^{-i2\pi\mathbf{u}_i l} \text{FT}_{\mathbf{u}_p} \left[\frac{1}{\tilde{B}(\mathbf{u}_p)} \right] * \text{FT}_{\mathbf{u}_p} [\tilde{M}_{\mathbf{u}_i}^{gu}(\mathbf{u}_p)] \quad (55)$$

and $\text{FT}_{\mathbf{u}_p} [\tilde{M}_{\mathbf{u}_i}^{gu}(\mathbf{u}_p)]$ can be developed as:

$$\text{FT}_{\mathbf{u}_p} [\tilde{M}_{\mathbf{u}_i}^{gu}(\mathbf{u}_p)] = \text{FT}_{\mathbf{u}_p} [\tilde{V}^{gu}(\mathbf{u}_p, \mathbf{u}_i)] = \quad (56)$$

$$= \text{FT}_{\mathbf{u}_p} [[\tilde{V}(\mathbf{u}_p, \mathbf{u}_i) S_{\mathbf{u}}(\mathbf{u}_i)] * G_{\mathbf{u}}(\mathbf{u}_i)] = \quad (57)$$

$$= [V(\mathbf{l}_p, \mathbf{u}_i) S_{\mathbf{u}}(\mathbf{u}_i)] * G_{\mathbf{u}}(\mathbf{u}_i) \quad (58)$$

Looking Eqs. 52, 55 and 58 it is clear that the equations are much more complex than in the standard imaging presented in Sect. 3.1. In particular, the gridding convolution kernel is "frozen" in the visibility maps.

6 Discussion of the different methods and summary

We have discussed the measurement equations for interferometric mosaicing in pointed mode (the so-called stop-and-go or point-and-shoot mosaics) and in on-the-fly (OTF) mode, in which the antennas take data as they scan the source moving continuously. We have shown that OTF mosaicing is similar to classical stop-and-go mosaicing. The main difference is that the effective beam when observing OTF is not exactly the primary beam of the antennas. However, the effective beam is similar to the primary beam when the scanning rate is better than Nyquist.

Regarding the imaging techniques, first we have discussed map size and observing time limitations for OTF mosaicing. OTF mosaics with ALMA are limited, in general, to a few arcminutes. Next, we have shown that it is possible to image and deconvolve OTF mosaic

data as a classical stop-and-go mosaic with a large number of fields. The joint deconvolution is known to recover some of the spatial frequencies that are averaged in each baseline (Cornwell et al. 1993). However, it is worth-trying to implement an OTF-specific algorithm based on the ER79 scheme, since it will synthesize explicitly the visibility of the source at those frequencies. We have explored two possible ways of implementing such an algorithm: beginning by Fourier transforming the data with respect to the pointing coordinate or beginning by gridding the data in the individual uv-planes corresponding to the different fields/dumps. In principle it seems simpler to start by gridding the uv-planes: it is already done in standard imaging techniques and thus it avoids coding specific algorithms to sort the visibilities baseline per baseline in temporal series to determine which visibility measurements in each mosaic field correspond to the same uv point. In addition, taking into account the short integrations needed to do wide field imaging in OTF mode, beginning by gridding the uv-planes has the advantage of increasing the signal to noise ratio by averaging visibility samples within the same uv cell. However, to image the whole mosaic at once it is important to use small \mathbf{u} cells (the cell size should be inversely proportional to the mosaic size). For instance, if the mosaic linear size is 4' the cell size should be $0.85 \text{ k}\lambda$ (2.5 m for observations at 3 mm). As shown in Table 1 and discussed in Sect. 4, there is a maximum observing time of 8.8 minutes for such a mosaic, corresponding to a minimum scanning velocity $v_{scan}=5 \text{ arcsec/sec}$ (which implies a dumping time of 2 sec to have four points per FWHM at 3 mm). With these observing time and scanning velocity, there will be only one visibility measured per cell in the largest baselines (92m for the PdBI in D configuration) but of course an average of 2 points per cell at a radius of 45 m or 4 points at 22 m, which is about the shortest spacing measured at the Plateau de Bure Interferometer, for example. In order to have a factor of two more points per cell it will be necessary to scan at 10 arcsec/sec and complete the map in 4.4 minutes. However, in this case the dumping time should be shorter by a factor of 2 (1 sec), therefore the total integration time per cell will be constant and the noise per cell will not be lower than using $v_{scan}=5 \text{ arcsec/sec}$. Therefore, only for the shortest baselines there would be a real gain in the signal to noise ratio. In addition, for those spacings, there is a higher probability to have \mathbf{u} points of different tracks laying in the same \mathbf{u} cell.

In addition, when beginning by gridding the uv-planes one should be sure that it is possible to correct for the convolution by the gridding kernel in later stages of the data processing. At this stage, it is not clear whether this is possible. An alternative method is to begin by Fourier transforming the data with respect the pointing coordinates, to compute a global uv-plane and to perform an standard imaging (including gridding) and deconvolution.

7 Bibliography

- Boone F., 2002, ALMA memo 400
- Bridle, A. H., & Schwab, F. R. 1999, in G. B. Taylor, C.L. Carilli and R.A. Perley (Eds.), *Synthesis Imaging in Radio Astronomy II*, 371
- Briggs. D.S., & Schwab, F. R., Sramek R.A., 1999, in G. B. Taylor, C.L. Carilli and R.A. Perley (Eds.), *Synthesis Imaging in Radio Astronomy II*, 371
- Cornwell T.J., 1987, ALMA memo 42
- Cornwell, T. J. 1988, *A&A*, 202, 316
- Cornwell, T., Braun, R., & Briggs, D. S. 1999, in G. B. Taylor, C.L. Carilli and R.A. Perley (Eds.), *Synthesis Imaging in Radio Astronomy II*, 151
- Cornwell T.J., Holdaway M.A., Uson J.M., 1993, *A&A* 271, 697
- Cotton, W. D. 1999, in G. B. Taylor, C.L. Carilli and R.A. Perley (Eds.), *Synthesis Imaging in Radio Astronomy II*, 357
- D’Addario L.R. & Emerson D. T., 2000, ALMA Memo 331
- Ekers R.D. & Rots A. H., 1979, in C. van Schooneveld (Ed.), *Image Formation from Coherence Functions in Astronomy*
- Ge, Jing Ping, 1992, ALMA memo 80
- Gueth 1997, PhD Thesis, Université Joseph Fourier
- Gueth 2000, in A. Dutrey (Ed.), IRAM Millimeter Interferometry School
- Guilloteau S., 2000, in A. Dutrey (Ed.), IRAM Millimeter Interferometry School
- Helfer, T. T., Vogel, S. N., Lugten, J. B., & Teuben, P. J. 2002, *PASP*, 114, 350
- Holdaway M.A., 1996, ALMA memo 156
- Holdaway M.A., 1997, ALMA memo 172
- Holdaway M.A., 1999, in G. B. Taylor, C.L. Carilli and R.A. Perley (Eds.), *Synthesis Imaging in Radio Astronomy II*, 401
- Holdaway M.A. & Foster S.M.. 1994, ALMA memo 122
- Holdaway M.A. & Rupen M.P. 1995, ALMA memo 128
- Kogan L.R., 1997, ALMA memo 171
- Morita K.-I., 2001, ALMA memo 374
- Pety J., Gueth F., Guilloteau S., 2001c, ALMA memo 386
- Pety J., Gueth F., Guilloteau S., 2001a, ALMA memo 387
- Pety J., Gueth F., Guilloteau S., 2001b, ALMA memo 398
- Perley, R. A. 1999, in G. B. Taylor, C.L. Carilli and R.A. Perley (Eds.), *Synthesis Imaging in Radio Astronomy II*, 383
- Rodríguez-Fernández, N.J., Pety J., Gueth J. 2008, IRAM memo 2008-2
- Rodríguez-Fernández, N.J., Gueth J., Pety J., 2009 IRAM memo 2009-3
- Tsutsumi T., Morita, K.-I., Hasegawa T., Pety J., 2004, ALMA memo 488
- Wright M. C. H., 1996, BIMA memo 45
- Yun M., 2001, ALMA memo 368